PHYSICAL REVIEW APPLIED **11,** 024022 (2019)

Ultrasparse Acoustic Absorbers Enabling Fluid Flow and Visible-Light Controls

Taehwa Lee,[*] Tsuyoshi Nomura, Ercan M. Dede, and Hideo Iizuka
Toyota Research Institute of North America, Toyota Motor North America, Ann Arbor, Michigan 48105, USA

(Received 21 September 2018; revised manuscript received 26 December 2018; published 8 February 2019)

Manipulation of acoustic waves, in particular for perfect absorption through a subwavelength medium, is of great importance in scientific and practical aspects. Conventional absorbers (e.g., thick foams or dense media) can sufficiently absorb acoustic waves, but at the same time, block fluid flow and visible light. Although sparsely arranging acoustic resonators will permit fluid flow and light propagation, this sparse arrangement leads to high acoustic transmission because of acoustic radiation symmetry. We analytically and numerically demonstrate that a sparsely distributed resonator array consisting of pairs of lossy and lossless resonators has perfect absorption at resonance with ultrahigh sparsity (a volume-filling ratio of <5%) owing to the symmetry breaking induced by the asymmetric loss. We find that the maximum period for ultrahigh sparsity is bounded by four times the absorption cross-section limit of a single-resonance subwavelength resonator, independent of its physical dimensions. Therefore, one can, in principle, obtain arbitrarily high sparsity. We experimentally demonstrate that our sparse absorber array exceeds 90% absorption at resonance with a volume-filling ratio of approximately 26%. In addition, we show that the ultrasparse absorber enables air-flow-direction control and optical cloaking. These results open up an area of multidisciplinary, multifunctional acoustic metamaterials.

DOI: 10.1103/PhysRevApplied.11.024022

I. INTRODUCTION

Acoustic metamaterials enable unprecedented control and manipulation of sound waves, allowing a myriad of exotic applications [1–5]. In particular, absorbing media for acoustic waves are of emerging importance from both scientific and practical perspectives, and systematic inclusion of lossy media in metamaterials enables design of acoustic metamaterials in the complex domain (e.g., parity-time symmetry [6,7], realization of a coherent perfect absorber (CPA) [8,9], and critical coupling for perfect absorbers [10–12]). Among these demonstrations, noteworthy progress has been made in realizing ultrathin perfect absorbers for noise control [13–21]. Optically transparent or fluid-permeable sound-absorbing panels will enable many potential applications such as reduction of noise from cooling fans or at the outlet of ductwork, and transparent noise barriers for architects or on highways without using transparent materials. Microperforated acoustic absorbers have demonstrated the usefulness of fluid-permeable sound-proofing panels [22], but with limited fluid permeation. In Ref. [23], the fluid permeability was significantly increased with an ultrasparse reflective metasurface using Mie scattering resonators. Although such reflectors can isolate an area from sound propagation, this solution often exacerbates the noise issue at the point of origin (e.g., noise sources in enclosures). Thus, absorption-type ultrasparse metamaterials are highly desirable.

It is extremely challenging to realize absorption-type metamaterials with an ultrahigh sparsity (volume-filling ratio $< 10\%$). For a periodic array of unit cells, its volume-filling ratio is conservatively defined as the ratio of the maximum lateral width of each unit cell to the period of the unit cells. Evidently, the reported absorption-type acoustic structures [14,24,25] show only limited sparsity with volume-filling ratios of $>70\%$. Intuitively, high sparsity gives rise to considerable acoustic-wave transmission, thereby limiting the maximum absorption to 50% because of the symmetry argument [26,27], where subwavelength single-resonance resonators lead to symmetric scattering in the forward and backward directions. Because of such a symmetry argument, the ultrasparse reflector based on monopole radiation [23] cannot be simply converted into a sparse absorber by inclusion of a loss effect [28]. Moreover, even for a sparse absorber with no transmission, it remains an open question as to whether the sparsity of the absorber is comparable to that of the sparse reflector reported in Ref. [23]. This question arises since the maximum absorption cross section of each subwavelength resonant unit, likely related to the sparsity, is four times smaller than its maximum scattering (reflection) cross section [29].

Here, we analytically and numerically show that a sparsely distributed resonator array has perfect absorption at resonance with ultrahigh sparsity (i.e., a volume-filling ratio of $< 5\%$). Such perfect absorption is realized with

---

[*] taehwa.lee@toyota.com

a pair of lossy and lossless resonators capable of symmetry breaking and strong resonance coupling. The perfect absorption is obtained for periods up to approximately $2\lambda/\pi$, which is determined by four times the upper limit of the absorption cross section of a subwavelength single-resonance resonator, $4\sigma_{\text{abs}}^{o}(= 2\lambda/\pi)$, independent of the physical dimensions of the resonator. Therefore, we can, in principle, obtain arbitrarily high sparsity. It is experimentally demonstrated that the absorption of the one-dimensional (1D) sparse array exceeds 90% with high sparsity (a volume-fill ratio of approximately 26%). Such high sparsity renders our absorbers versatile by enabling fluid flow and visible-light controls. Simultaneously, we highlight air-flow-direction control via an array of fish-shaped sparse absorbers. We further present the feasibility of combining sparse absorbers with an invisible cloaking technique through the use of mirror coatings for an optically transparent acoustic absorber without the exclusive use of transparent materials.

II. EXPERIMENTAL SETUP AND SIMULATION

A. Device fabrication

Our sparse absorber is composed of a periodic array of two-sided Helmholtz resonators (HRs), as shown in Fig. 1(a). We fabricate two types of sparse absorbers (Type I, fish shape; Type II, double-diamond shape). For both types, each unit cell consists of lossy and lossless HRs operating at the same resonance frequency. Without introducing any lossy medium, the loss of the HRs is adjusted by varying the lengths of the necks (l_n), where viscous losses occur due to the friction of the oscillating air in the neck region. For given neck lengths (l_n) for desired loss, the neck width (w_n) and cavity area (S_c) of the HRs are chosen to maintain the same resonance frequency (f_0) in the HR pair, that is, $f_0 \propto \sqrt{w_n/S_c l_n}$. For Type I, the dimensions of the front lossy HR are given by $w_{n,F} = 0.6$ mm, $l_{n,F} = 4$ mm, and $S_{c,F} = 58$ mm^2, while those of the back lossless HR are given by $w_{n,B} = 1.1$ mm, $l_{n,B} = 2$ mm, and $S_{c,B} = 94$ mm^2, and the subscripts F and B representing the front and back, respectively. The lateral width and length of the HR pair are given by $w = 10$ mm and $h = 31$ mm. For an optically transparent acoustic absorber (Type II), the unit absorber is modified to a double-diamond shape and its surface is coated with mirrors (First Surface Mirror LLC, Toledo, OH, USA). The mirror width ($l_M = 10$ mm) is given by $l_M = h/4\cos\theta_M$ with h the length (y direction) of each unit and θ_M the angle of the mirrors with respect to the y axis (see Fig. S1 in the Supplemental Material [30]). Here, the angle θ_M is numerically determined with $d - (h/4)\tan\theta_M = (h/4)\tan 2\theta_M$ for a given period (d) and length (h). For Type II, the dimensions of the front lossy HR are given by $w_{n,F} = 0.55$ mm, $l_{n,F} = 4$ mm, and $S_{c,F} = 42$ mm^2, while those of the back lossless HR are given by $w_{n,B} = 0.7$ mm, $l_{n,B} = 2.5$ mm, and $S_{c,B} = 88$ mm^2. The sparse absorbers are fabricated by using a fused-deposition-molding (FDM) style three-dimensional (3D) printer (model Markforged Mark Two, Markforged Inc., MA, USA) with a 400-μm-nozzle diameter and 100-μm-layer height. The printing material is made of a chopped carbon-fiber-filled nylon composite with 1.4 GPa tensile modulus and 1.18 g/cm^3 density. The parts are additively manufactured with 100% fill factor without continuous fiber reinforcement.

B. Acoustic measurement

Acoustic performance is characterized with an in-house impedance tube measurement system based on the four-microphone measurement method, consisting of a square tube (40×40 mm^2), a full-range speaker (2½″, model SB65WVAC25-4, SB Acoustics, http://www.sbacoustics.com/), pressure-field microphone and preamplifier (¼″ prepolarized, sensitivity 1 mV/Pa, model 378C10, PCB Piezotronics, NY, USA), audio power amplifier (model APA150, Daytonaudio), data acquisition device (24-bit, 102.4 kS/s, model NI USB-4431, National Instruments), and pyramid-shaped anechoic termination (polyurethane foam). The schematics of the measurement setup are found in Note 2 in the Supplemental Material [30]. The measured signals are processed with MATLAB data acquisition toolbox (Mathworks, MA, USA).

C. Air flow experiment

Flow visualization in air is conducted in an in-house smoke tunnel consisting of a test section ($70 \times 70 \times 500$ mm^3) and a fan (3.49×10^{-2} m^3/s, model SP120L, Corsair) attached to a flow diffuser (diverging angle 3.5°) in downstream, and a settling chamber (20-mm-thick honeycomb) with contraction in upstream (see Fig. S3 in the Supplemental Material [30]). Smoke for flow visualization is generated by burning sticks. The flow speed of the fan is controlled by a varying voltage (0–12 V) from a dc power supply (GPS-3303, Goodwill Instrument CO., LTD). For demonstration of flow-direction control, five absorber columns are placed in front of the same fan, and three flow indicators (red flags) are placed downstream of the absorbers (see Fig. S4 in the Supplemental Material [30]).

D. Simulations

All simulations are conducted by using a commercial finite-element-method (FEM) solver (COMSOL Multiphysics 5.3). For acoustic simulations, an acoustic module combined with a structural module is used, and the loss of HRs is considered by using the Thermoviscous Acoustic Interface in COMSOL Multiphysics. For fluid-flow simulation, fluid flow around the sparse absorber in a duct is simulated by solving a two-dimensional Navier-Stokes

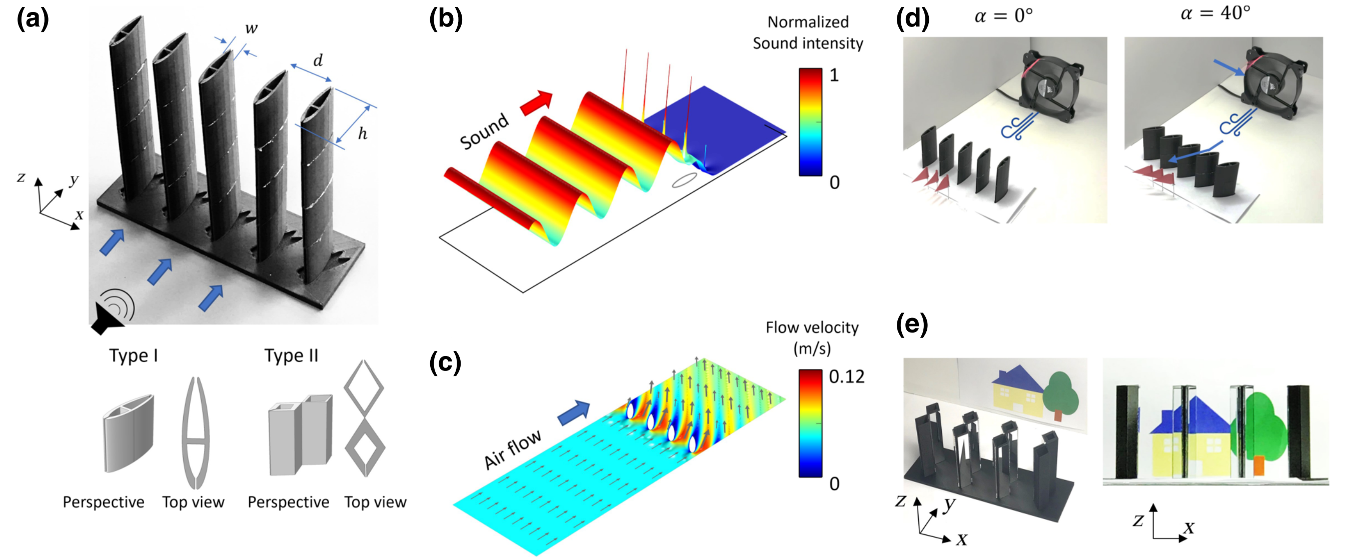

FIG. 1. Multifunctional sparse acoustic absorbers. (a) 3D-printed sparsely arranged acoustic absorber (Type I. fish shape) with a volume-filling ratio of 26%, enabling fluid-flow control. The five unit cells are attached to the bottom plate with grooves for different tilting angles, while the cover plate is removed to see the inner structure. For visible-light control, the unit cells are replaced with Type II (double-diamond shape). (b) Simulated sound intensity for the fish-shaped resonator array (Type I), normalized to the incident sound intensity. (c) Simulated flow velocity field for the tilted fish-shaped resonator array, subjected to laminar air flow (a uniform input flow velocity of 0.05 m/s). (d) Demonstration of fluid-flow direction control (Type I) for two angles of attack ($\alpha = 0°, 40°$) (see Video 1 in the Supplemental Material [30]). (e) Demonstration of invisible sparse absorbers with optical cloaking (Type II), showing that the two center columns coated with mirrors are invisible.

equation. In this simulation, at the inlet of the duct, a constant velocity is used and the outlet pressure is set as a zero gauge pressure. In addition, flow angle (θ_F) is characterized with $\theta_F = \tan^{-1}(|\int_0^d u dx / \int_0^d v dx|)$, where d is the period of the unit cells and u and v are the velocity components in the x and y directions, respectively. For the optical-cloaking device, ray-tracing simulation is performed by using twenty rays for each period of the array. The mirrors on the Type-II device are modeled as perfect visible-light reflectors.

III. RESULTS AND DISCUSSION

A. Multifunctional ultrasparse absorbers

A sparsely distributed, single-resonance HR array (volume-filling ratio of $>50\%$) allows considerable acoustic transmission due to the symmetry argument [26,27]. To break the symmetry for perfect absorption, we construct an ultrasparse acoustic absorber with a 1D array of pairs of lossy and lossless HRs. Such an asymmetric loss uniquely enables perfect absorption, whose mechanism will be discussed later. Figure 1(a) shows a 3D-printed prototype of a fish-shaped resonator array (Type I) composed of five unit cells along the x direction with a period of $d = 0.25\lambda_0 (\lambda_0 = 155$ mm at $f_0 = 2.2$ kHz). The width (w) and length (h) of each unit cell are $w = 0.06\lambda_0$ and $h = 0.2\lambda_0$, respectively, and the corresponding volume-filling ratio (w/d) is 26%. Each unit cell consists of two chambers (cavities) split by a thin wall, and these chambers with necks constitute lossy and lossless HRs. The lossy HRs have a relatively long neck ($l_{n,F} = 4$ mm) compared to the lossless HRs ($l_{n,B} = 2$ mm). For this sparse absorber, a specific shape (i.e., fish shape) and volume-filling ratio are selected to demonstrate an additional capability to control fluid flow. For optical control, the shape of the unit absorber may be modified to resemble a double-diamond-shaped absorber [Type II, Fig. 1(a)], while the neck responsible for losses remains longer than the lossless neck. Because of its subwavelength size ($< 0.2\lambda_0$), such a change in the shape of the unit absorber does not significantly affect the acoustic performance as long as the absorber has a similar length (h) and volume-filling ratio (w/d).

The fish-shaped absorber array exhibits excellent sound-absorbing characteristics, while enabling fluid-flow control. The sound intensity field around the absorber array is calculated by using the COMSOL simulator. Acoustic measurement is conducted by using a unit cell placed inside an impedance tube with a square cross section (40×40 mm^2), whose lateral width is equal to the period of the unit cells. Figure 1(b) shows the simulated sound-intensity field normalized to the incident-sound intensity. The opening to the lossy HR is directed toward the sound source, while the opening for the lossless HR is oriented away from the source. Despite the ultrahigh sparsity, sound intensity in the region behind the periodic absorbers is negligibly low with an insertion loss of 100%. Such significant sound reduction results from high absorption (approximately 97% in simulation), which is verified with the experimental results, showing a near-unity acoustic absorption of 91% at resonance ($f = 2.2$ kHz). To demonstrate a capability to control fluid-flow direction, a flow velocity field is simulated (COMSOL) for the fish-shaped absorbers titled at an angle of 40° under a constant-flow velocity, as shown in Fig. 1(c). We observe that flow direction is changed toward the orientation of each HR pair.

The operation frequency of the ultrasparse absorber is tunable such that it can be designed to absorb low-frequency sound (<500 Hz) by scaling up the sparse absorber. The relatively high operation frequency used in this study is chosen for demonstration of a proof of concept by using an impedance tube size comparable to those of standard impedance tubes. In addition, the ultrasparse acoustic absorber is unique in several aspects compared to other sound-proofing metamaterials. In particular, the ultrasparse absorber has negligible reflection, which is different from the reflection-type sparse metasurface [23], where any reflection may cause unwanted resonance by forming standing waves between the sound sources and the metasurface. The sparse absorbers with the lossy-lossless pairs allow significantly increased sparsity compared to other fluid-permeable (absorption-type) acoustic metamaterials [24,25]. Such ultrahigh sparsity makes our absorber versatile by experimentally demonstrating fluid-flow control [Fig. 1(d)] and optical cloaking [Fig. 1(e)]. In Fig. 1(d), an array of fish-shaped resonators (Type I) is tilted (angles of attack $\alpha = 0°$, 40°) to control the air flow direction from a fan (see Video 1 within the Supplemental Material [30]). In Fig. 1(e), an optically invisible absorber is demonstrated by mirror-coated double-diamond-shaped resonators (Type II), as the photograph of the resonators and the background illustration shows that the two center columns are optically transparent. Further details will be discussed after investigating the mechanism behind the ultrasparse absorption.

B. Sparsity limit of lossy-lossless resonators

Fundamental questions arise; for example, what is the mechanism behind the perfect absorption with such ultrahigh sparsity, and what is the limit of the sparsity? To answer these questions, we consider a harmonic-oscillator model composed of lossy-lossless oscillators of the same mass (m) and spring constant (k), as an equivalent model of the HR pair [Fig. 2(a)]. The coupled equation of motion of the harmonic oscillator pair is described by [31,32]

$$m\frac{d^2}{dt^2}\begin{bmatrix} x_1 \\ x_2 \end{bmatrix} + \frac{d}{dt}\begin{bmatrix} \eta_l + \eta_r & \eta_{12} \\ \eta_{12} & \eta_r \end{bmatrix}\begin{bmatrix} x_1 \\ x_2 \end{bmatrix} + \begin{bmatrix} k & 0 \\ 0 & k \end{bmatrix}\begin{bmatrix} x_1 \\ x_2 \end{bmatrix} = \begin{bmatrix} F_1 \\ F_2 \end{bmatrix}, \qquad (1)$$

where the subscripts represent each resonator (i.e., 1, lossy; 2, lossless), x_i is the oscillation amplitude, η_l is the internal loss, η_r is the radiation leakage loss, η_{12} is the radiation coupling between the lossy and lossless oscillators ($\eta_{12} = \eta_{21} = \eta_c$ by reciprocity), and F_i is the force acting on the oscillator. Note that Eq. (1) is valid for both an isolated pair and a unit cell of the oscillator pairs in an array. For a 1D array, the contributions of all the oscillator pairs can be considered through the leakage loss (η_r) and radiation coupling (η_c), which are complex values when the period of subwavelength resonators ($w \ll \lambda_0$) is comparable to the wavelength ($d \sim \lambda_0$) [33].

Using Eq. (1) with the vibration amplitude ratio of $X_{21} (= x_2/x_1)$ and complex values of η_r and η_c, the absorption (power) coefficient of the 1D array of the oscillator pairs is derived as

$$A(\omega) = 4\left(\frac{\eta_r^o}{\eta_0}\frac{\eta_l}{\eta_0}\right)\left\{\left[\frac{\omega}{\omega_0} - \frac{\omega_0}{\omega} + 2\,\mathrm{Im}\left(\frac{\eta_r + \eta_c X_{21}}{\eta_0}\right)\right]^2 + 4\left[\frac{\eta_l}{\eta_0} + \mathrm{Re}\left(\frac{\eta_r + \eta_c X_{21}}{\eta_0}\right)\right]^2\right\}^{-1}, \quad \text{and} \qquad (2a)$$

$$X_{21} = \left[\frac{\left(\frac{-\omega}{\omega_0} + \frac{\omega_0}{\omega}\right)\eta_0 + 2i(\eta_l + \eta_r - F_{12}\eta_c)}{\left(\frac{-\omega}{\omega_0} + \frac{\omega_0}{\omega}\right)\eta_0 + 2i(\eta_r - F_{21}\eta_c)}\right] F_{21}, \qquad (2b)$$

where $\omega_0 = \sqrt{k/m}$ is the resonance frequency (rad/s), $\eta_0 = 2\sqrt{km}$ is the critical damping coefficient (kg/s), and η_r^o is the reference leakage loss of a resonator with no acoustic transmission for $d < \lambda_0$, given by $\eta_r^o = ZS_{\mathrm{osc}}^2/S_{\mathrm{inc}}$ with Z the acoustic impedance, S_{osc} the area of the mass, and S_{inc} the area of the unit cell. Here, the use of X_{21} [Eq. (2b)] makes Eq. (2a) intuitive and helps to gain insight into resonance coupling. The imaginary part of $[(\eta_r + \eta_{21}X_{21})/\eta_0]$ represents a shift in the resonance of the oscillator array due to the radiation coupling [34], whereas the real part determines absorption. The detailed derivation is found in Appendix A.

For the design of the ultrasparse absorber, we use the unity absorption condition that is deduced from Eq. (2a) at resonance as $A = (\eta_r^o\eta_l)/[\eta_l + \mathrm{Re}(\eta_r + \eta_c X_{21})]^2$. One can check that perfect absorption occurs when the conditions of $\eta_l \approx \eta_r^o$ (critical coupling) and $\mathrm{Re}(\eta_r + \eta_c X_{21}) \approx 0$ are simultaneously satisfied. The later condition represents the complete cancellation of the leakage loss due to the coupling with the lossless resonator; the phase angle of each term should be out-of-phase [35,36], that is, $\arg(\eta_r) - \arg(\eta_c X_{21}) \approx \pi$. Physically, this states that the cancellation of the leakage loss increases the vibration amplitude of the lossy resonator, since the leakage loss dampens the vibration of resonators. Such interaction between the front and back resonators shares a common feature with

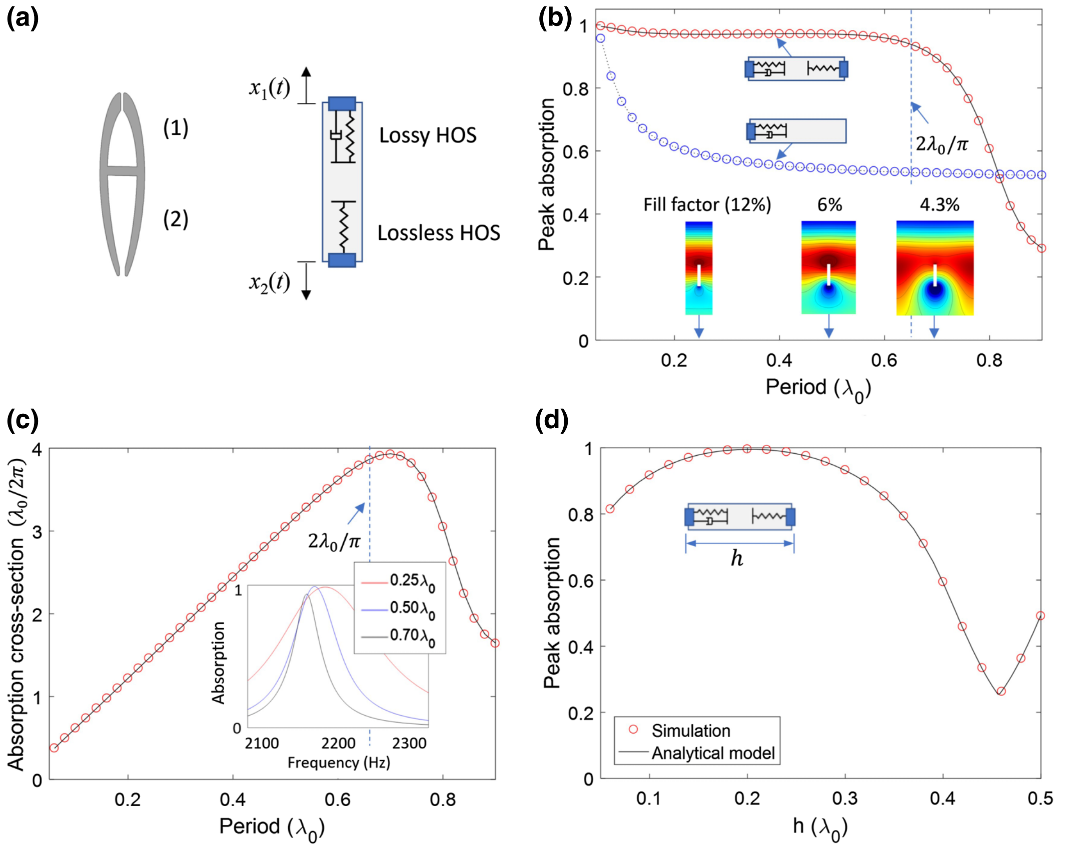

FIG. 2. Sparsity limit of acoustic absorbers. (a) Equivalent harmonic oscillator model (spring-mass-damper) of a pair of Helmholtz resonators. The oscillators, placed on the top and bottom surfaces of the sound-reflecting, vacuum-filled rectangular enclosure, are composed of identical masses and springs, and only the top oscillator includes a damper for asymmetrical loss. (b) Peak absorption with respect to the period (d) for the lossy-lossless oscillator pairs and single lossy oscillators. The same width ($w = \lambda_0/35$) and length ($h = 0.2\lambda_0$) are used. The symbols represent the numerical results while the solid lines indicate the analytical results. The inset shows the pressure fields for three representative periods ($d = 0.25\lambda_0,\ 0.5\lambda_0,\ 0.7\lambda_0$) and the corresponding volume-filling ratios of 12%, 6%, and 4.3%, respectively. (c) Absorption cross section of the lossy-lossless oscillator pairs with respect to the period. The absorption cross section is normalized to the maximum absorption cross section of an isolated single-resonance resonator, $\lambda_0/2\pi$ (subwavelength single-resonator limit). The inset shows the absorption spectra for $d = 0.25\lambda_0,\ 0.5\lambda_0,$ and $0.7\lambda_0$. (d) Peak absorption as a function of the length (h) between the lossy and lossless oscillators.

acoustic-dipole resonance, where dual resonances of opposite phases interact with each other [37]. To maximize the leakage cancellation, in addition to the phase requirement, a large $X_{21}(= x_2/x_1)$ is required. In this regard, the resonator pair with the lossy-lossless combination is an excellent choice because it has high x_2 (lossless) relative to x_1 (lossy), compared to a resonator pair with symmetrical loss (lossy-lossy).

To investigate the period limit, the peak absorption of the lossy-lossless oscillator array ($w = \lambda_0/35, h = 0.2\lambda_0$) is calculated as a function of the period (d). By using the COMSOL simulator, the acoustic response of the oscillator pair is numerically calculated under periodic boundary conditions, and the pair is modeled as a rectangular-shaped sound reflector with two vibrating masses attached on the top and bottom surfaces of the rectangular reflector [Fig. 2(a)]. The top rigid mass for a lossy oscillator has a spring and a damper as a spring boundary condition, whereas the bottom rigid mass for a lossless oscillator has only a spring. For each period (d), the internal loss (η_l) is adjusted to ensure critical coupling ($\eta_l \approx \eta_r^o = Zw^2/d$). Remarkably, the lossy-lossless HR pair shows near-unity absorption ($A > 0.9$) for periods up to $d \sim 0.7\lambda_0$, as shown in Fig. 2(b). We confirm that the condition of $\mathrm{Re}(\eta_r + \eta_c X_{21}) \approx 0$ is satisfied. The numerical results (symbols) show excellent agreement with the analytical results (lines) obtained with Eq. (2). For the analytical results, we use the leakage loss (η_r) and radiation coupling (η_c) that are numerically retrieved [38] (A detailed calculation of these terms is found in Appendix B). In contrast, the peak absorption of the single-resonance oscillator (lossy alone; $x_2 = 0$) drastically decreases to approximately 50% upon increasing the period d, which can be verified by Eq. (2a) with $X_{21} = 0$ and the leakage loss

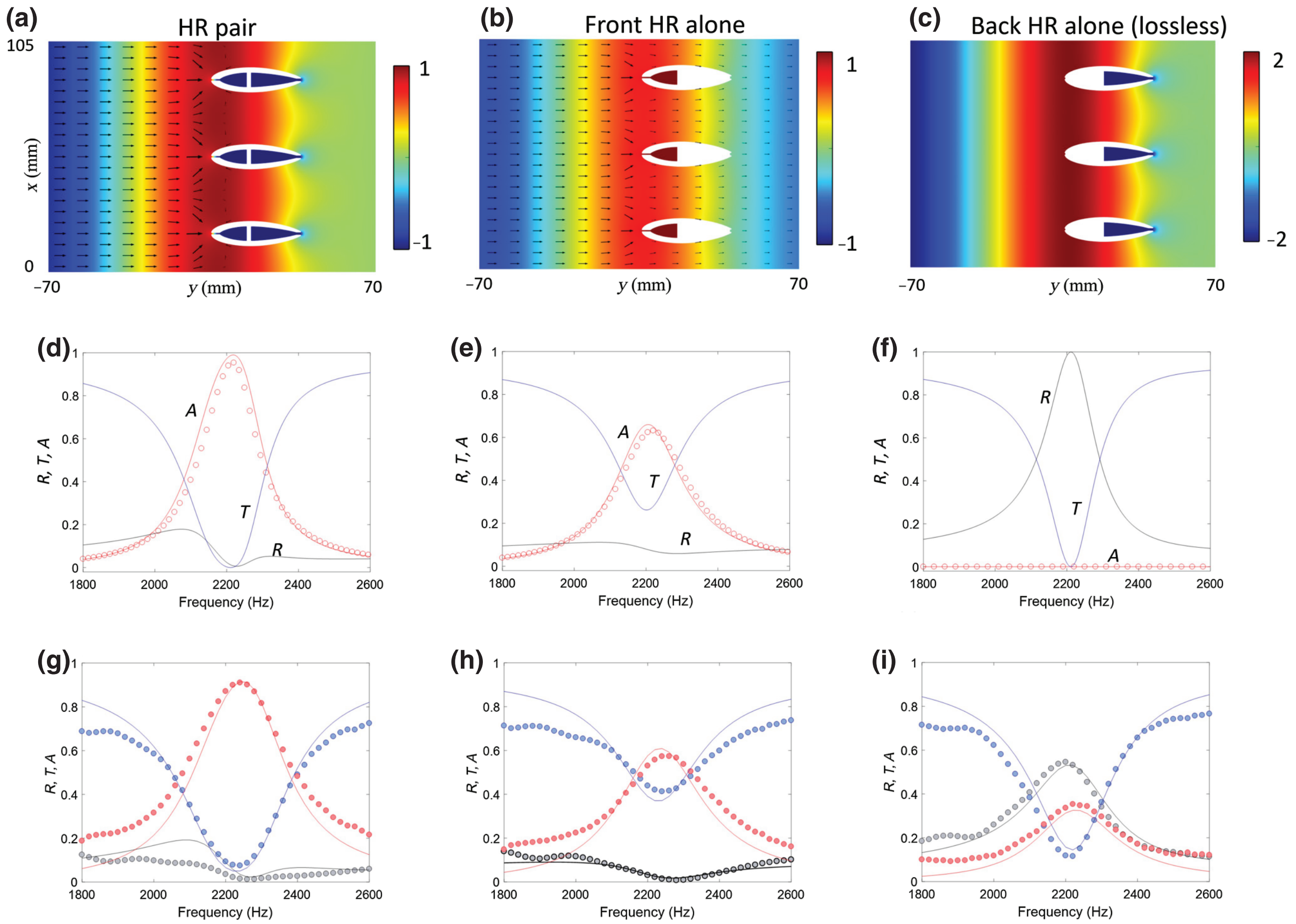

FIG. 3. Mechanism of unity absorption in sparse lossy-lossless resonators. (a) Simulated pressure field for an array of HR pairs. Pressure field, normalized to the incident pressure amplitude, is overlaid by acoustic energy flow (arrow). (b) Pressure field for an array of front lossy HRs. (c) Pressure field for an array of back lossless HRs (No acoustic energy flow is shown due to perfect reflection.). (d), (e), (f) Numerically calculated acoustic spectra (solid lines) for the HR pair array, front lossy HRs, and back lossless HRs, respectively: absorption (A), reflection (R), and transmission (T). For comparison, also plotted is the analytical absorption spectrum (red circle symbols) obtained with the harmonic oscillator model. (g), (h), (i) Measured acoustic spectra (symbols) for the HR pair array, front lossy HRs, and back lossless HRs, respectively. The numerically calculated acoustic spectra (solid lines) are obtained by considering non-negligible loss in the back HRs and adjusting loss in the front HRs.

$\mathrm{Re}(\eta_r) = \eta_l \approx 0.5\eta_r^o$, that is, $A = \eta_l\eta_r^o/(\eta_l + 0.5\eta_r^o)^2 \approx 0.5/(0.5 + 0.5)^2 = 0.5$.

The period limit can be clearly understood in terms of the absorption cross section, which defines the probability of an absorption process in sparsely distributed resonators. The absorption cross section of the periodic array is calculated with multiplication of the peak absorption (A) from Eq. (2a) and period (d), given by

$$\sigma_{\mathrm{abs}} = dA \approx d\left[1 + \mathrm{Re}\left(\frac{\eta_r + \eta_c X_{21}}{\eta_r^o}\right)\right]^{-2}. \tag{3}$$

Eq. (3) indicates the linear relation of $\sigma_{\mathrm{abs}} \approx d$ for the complete leakage cancellation and $\mathrm{Re}(\eta_r + \eta_c X_{21}) \approx 0$. Indeed, Fig. 2(c) shows such a linear relation. At the period limit of the near-unity absorption approximately $0.7\lambda_0$), we find that σ_{abs} has a maximum of σ_{max}, which is four times larger than that of a two-dimensional (2D) isolated single-resonance resonator with an isotropic angular response ($\sigma_{\mathrm{abs}}^o = \lambda_0/2\pi$) [29]. Such a large absorption cross section results from the upper limit of the scattering cross section of the lossless resonator within the lossy-lossless pair. Beyond the period limit, the coupling condition deviates from $\mathrm{Re}(\eta_r + \eta_c X_{21}) \approx 0$, leading to the decrease in both A and σ_{abs}.

The period limit ($0.7\lambda_0$), together with the small width ($w = \lambda_0/35$), results in ultrahigh sparsity with a volume-filling ratio of $w/d = 4.3\%$ [inset of Fig. 2(b)]. Note that the period limit depends on the resonance wavelength (λ_0), but it is independent of the physical cross section.

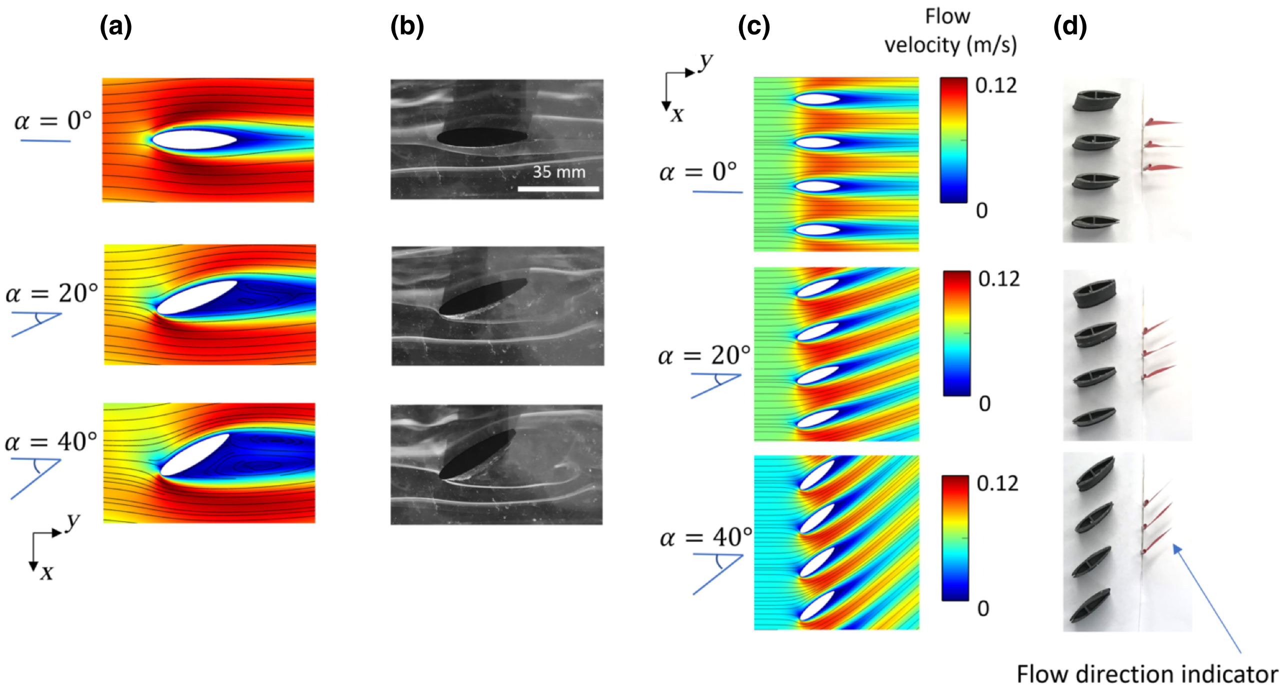

FIG. 4. Flow-direction control with sparse acoustic absorbers. (a) Flow simulation around a unit absorber between two parallel walls (separated by $0.25\lambda_0$). (b) Smoke test for flow visualization (see Videos 2–4 in the Supplemental Material [30]). (c) Flow simulation around the periodic array for angles of attack ($\alpha = 0°,\ 20°,\ 40°$). (d) Demonstration of flow-direction control for the same angles of attack [the perspective view of the entire system is shown in Fig. 1(d)]. The flow direction is real time captured with flow-direction indicators (red flags) (see Video 1 in the Supplemental Material [30]).

Therefore, one can, in principle, achieve arbitrarily high sparsity by decreasing the width (w) as long as resonance is maintained. The small width ($w = \lambda_0/35$) used in the oscillator model is a realistic value, allowing to convert it into an ultrasparse HR array (see Note 4 in the Supplemental Material [30]). Furthermore, the width can be further decreased by implementing the space-coiling approach used in subwavelength acoustic absorbers [17]. Although increasing the period is desirable in realizing high sparsity, it can compromise the absorption bandwidth. A larger period results in a smaller absorption bandwidth [inset of Fig. 2(c)], because it reduces the total loss (i.e., sum of leakage and internal losses) by decreasing both leakage loss $\eta_r^o = Zw^2/d$ and internal loss $\eta_l = \eta_r^o$ for critical coupling.

For the coupling of the two resonators, the length of the resonator pair (h) is a critical parameter. Figure 2(d) shows the peak absorption characteristic as a function of h for the array of the lossy-lossless harmonic oscillators. We find an optimum length between the resonators in the unit cell (i.e., $h = 0.2\lambda_0$). Based on the unity absorption condition [$\mathrm{Re}(\eta_r + \eta_c X_{21}) \approx 0$], the optimum length corresponds to the condition where $\mathrm{Re}(\eta_r + \eta_c X_{21})$ has the smallest positive value and $\mathrm{Re}(\eta_r) > 0$ and $\mathrm{Re}(\eta_c X_{21}) < 0$, that is, $\mathrm{Re}(\eta_r + \eta_c X_{21}) < \mathrm{Re}(\eta_r)$. Physically, such a condition indicates that the radiation leakage (η_r) from the lossy front resonator is cancelled by the lossless back resonator ($\eta_c X_{21}$).

The role of the back lossless resonator is studied in detail by decomposing each HR within the fish-shaped HR pair ($w/d = 26\%$, $h = 0.2\lambda_0$). Figure 3 shows the simulated pressure fields and the acoustic energy flows at resonance. For the HR pair, all of the acoustic energy (denoted by the proportionally scaled black arrows) goes into the lossy front HR [Fig. 3(a)]. The simulated absorption spectrum (solid red line in the lower image) of the HR pair shows perfect absorption at resonance and matches very well with the absorption spectrum (symbols) obtained from the oscillator model by using Eq. (2). Such perfect absorption in the HR pair comes from the back HR capable of preventing the wave transmission, which is otherwise observed for the front HR alone [Fig. 3(b)]. We find that, surprisingly, the back HR alone works as a perfect reflector (100% reflection) [Fig. 3(c)]. Here, the perfect reflection of the lossless resonator, which supports monopole resonance, is similar to that of Mie resonators showing perfect reflection in monopole resonance [23]. In other studies, lossy resonators implemented with planar reflectors have been widely used for perfect wave absorption in optics and acoustics [39–41], where no transmission occurs by the planar reflectors. Here, in our design, one of the two resonators

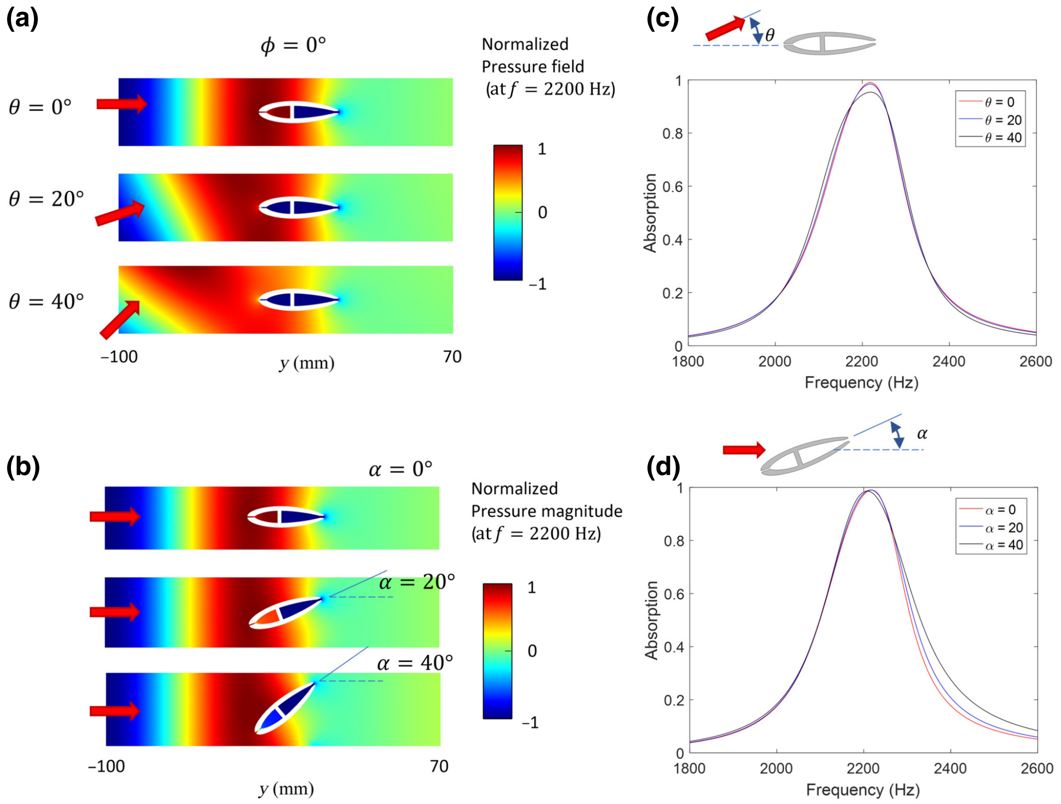

FIG. 5. Numerically calculated acoustic absorption [(a), (b) pressure distributions at 2200 Hz and (c), (d) frequency responses] depending on different incident angles (a), (c) and different attack angles (b), (d).

in the unit cell works as a reflector, allowing a sparse arrangement of the constituent resonators.

The numerically calculated near-perfect absorption [Fig. 3(d)] is compared with the measured absorption in Fig. 3(g), which shows approximately 91% absorption. The difference in the peak absorption comes from a non-negligible loss in the back HRs [Fig. 3(i)]. By considering the loss in the back HRs, the numerical results (solid lines) show a nice agreement with the experimental results (symbols). The loss in the back HRs can be reduced by increasing the neck width, which requires a larger volume of the cavity for the same resonance frequency.

C. Flow-direction control

A motivation for ultrahigh sparsity is to realize directional fluid-flow control in combination with near-unity acoustic absorption. Fluid-flow control using sparse acoustic absorbers will be useful in various applications. For instance, when sparse absorbers are used as directional vanes to reduce the noise from cooling fans or at the outlet of ductwork, the streamlined shape of the sparse absorbers should not significantly increase the electrical power consumption of such systems for maintaining a flow rate [42,43]. To demonstrate the capability of fluid-flow control, fluid flow around the sparse absorber in a duct is simulated by solving a steady-state laminar incompressible flow model in two dimensions (Navier-Stokes equation), where no-slip boundary conditions are applied to all surfaces except the inlet and outlet. At the inlet of the duct, a constant velocity is used and outlet pressure is set as zero gauge pressure. To verify the simulation results, flow visualization in air is conducted in an in-house smoke tunnel with smoke generated by burning sticks.

Our fish-shaped sparse absorbers (Type I) provide for minimal disruption-separation of fluid flow streamlines when subjected to laminar air flow (Reynolds number $N_{\mathrm{Re}} = \rho u h/\mu = 140 < 1800$, with u the flow velocity and μ the dynamic viscosity) at a zero angle of attack, $\alpha = 0$, as confirmed via the fluid-flow simulation in Fig. 4(a) and smoke test in Fig. 4(b) (see Videos 2–4 in the Supplemental Material [30]). In contrast, rectangular-shaped sparse absorbers with the same width (w) increase the drag force two fold (see Note 5 in the Supplemental Material [30]), although the acoustic performance of subwavelength resonators is not significantly affected by their shapes (see Note 6 in the Supplemental Material [30]). Tilting the sparse absorbers relative to the incoming flow enables active downstream control of flow direction (e.g., replacing the louvers of an air-conditioning unit). For this flow control, at higher angles of attack, for example, 20° and 40°, flow instability and separation are observed past the

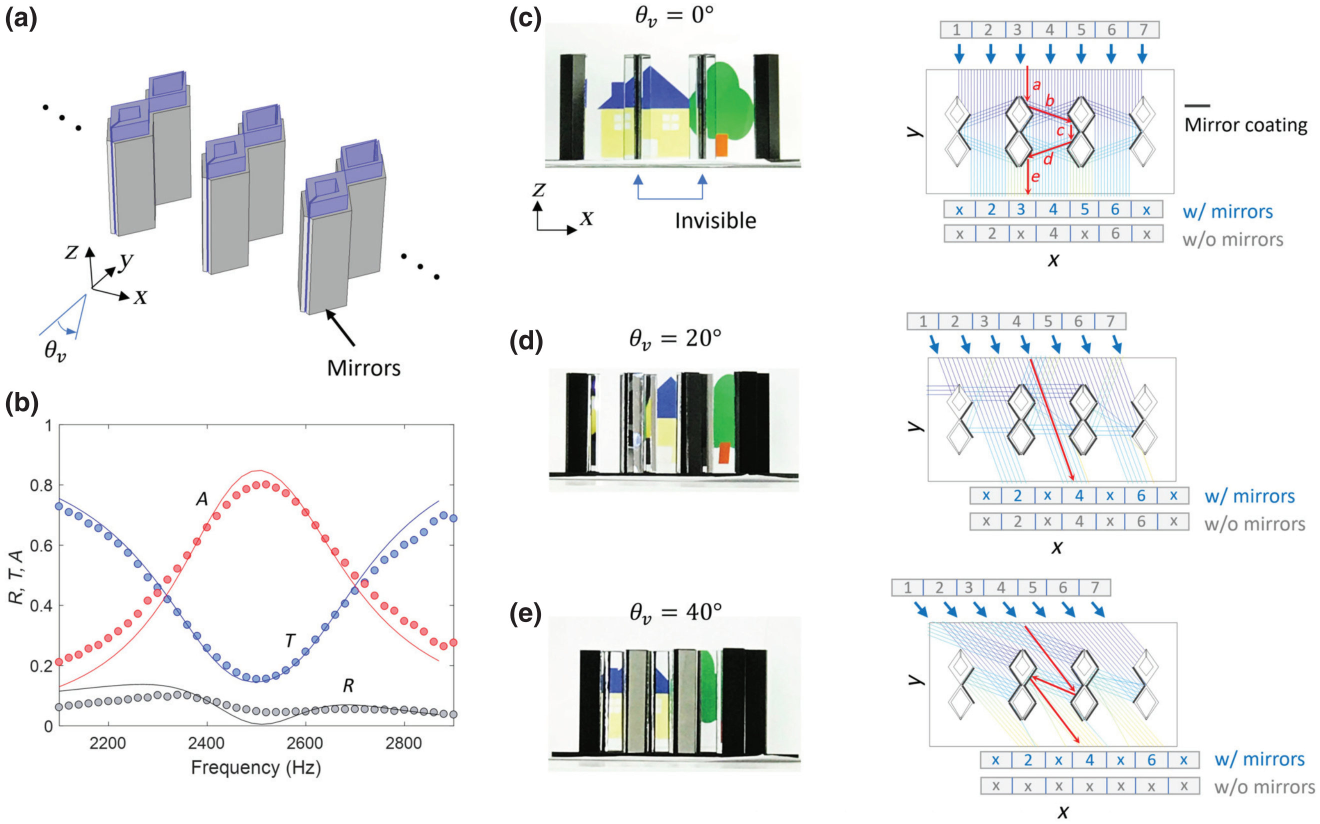

FIG. 6. Optically transparent acoustic absorbers. (a) Schematic of the double-diamond HR array coated with mirrors. Viewing angles (θ_v) are defined as a horizontal angle on the x-y plane. (b) Acoustic absorption (A), transmission (T), and reflection (R) of the unit cell. (c) Photographed image (normal view, $\theta_v = 0°$) of four HR columns with the two center columns invisible [the perspective view of the system is shown in Fig. 1(e)]. In the right panel, the corresponding ray simulation shows an example light path (red arrows labelled as *a*-*b*-*c*-*d*-*e*) due to reflection from the mirrors (thick black outlines). With and without mirrors, the bottom number labels of the ray simulation indicate the visibility of the incident light (blue arrows), virtually divided by the seven regions. In these labels, x indicates no visible light. (d) For an oblique view angle of $\theta_v = 20°$. (e) For an oblique view angle of $\theta_v = 40°$.

downstream surface of a single absorber both in simulations [Fig. 4(a)] and experiments [Fig. 4(b)]. Thus, to provide enhanced fluid-flow control, an array of absorbers with a period of $d = 0.25\lambda_0$ is considered, and simulations of fluid flow past this array indicate reduced flow separation with greater angular control of downstream fluid-flow orientation [Fig. 4(c)], showing that the simulated flow angle (θ_F) is equal to the angle of attack (α). The effectiveness of the array of sparse absorbers on fluid-flow control is further verified by experiments [Fig. 4(d)], where downstream flow indicators closely track the angle of attack of the absorber array (see Video 1 in the Supplemental Material [30]). Note that tilted sparse absorbers do not compromise the acoustic performance of the array. Figure 5 shows that the tilting of the absorber for fluid-flow control does not affect absorption performance. Moreover, the absorption of the fish-shaped absorber is insensitive to the angle of incident acoustic waves (up to 40°). Finally, although higher sparsity is good for fluid flow due to low-flow resistance, excessive sparsity negatively affects fluid-flow control. Hence, for flow control there is an absorber-spacing optimum condition where the flow orientation is equal to the angle of attack (see Note 7 in the Supplemental Material [30]).

D. Optically transparent acoustic absorber

By adding optical transparency to our sparse absorber, we can construct an optically transparent, fluid-permeable acoustic absorber, which is useful in various applications such as noise barriers on highways and soundproof windows. Our sparse absorber itself has a good visibility of 74% (=100 − 26% volume-filling ratio), and we show that the remainder of the 26% (i.e., resonators) may be hidden for an optically transparent acoustic absorber by including optical-cloaking technology. While invisibility cloaking investigations have been led by rigorous theories [44–46], hiding a large object is realized in the full visible region for simple structures composed of commercially available optical components such as lenses, mirrors, and polarizers when the omnidirectionality requirement is abandoned [47,48]. Here, we extend the invisibility cloak technique to a sparse periodic structure and implement it on our absorber. For optical cloaking, each HR pair is reconfigured into the double-diamond HR (Type II), whose faces are coated with eight flat mirrors of the same size ($60 \times 10 \times 1$ mm^3), as the schematic of the mirror-coated absorber is shown in Fig. 6(a). This specific shape is chosen for an even number of mirror reflections, allowing the incoming visible light to return to the original light path without an overall image flip. Our periodic cloaking technique does not compromise the sparsity of our acoustic absorber design, because it employs mirrors directly attached to the boundaries of the cloaking regions and takes advantage of mirrors on neighboring absorbers. With this diamond-shaped HR, high acoustic absorption (approximately 80%) is maintained and confirmed with the measurement (symbol) and the simulation results (line) [Fig. 6(b)].

The invisibility cloaking effect is experimentally verified using an array of 3D-printed four absorber columns with the two center columns fully mirror coated and the rest of the columns partially mirror coated. The absorber array and the background (printed illustration of a house and a tree) are photographed for different viewing angles ($\theta_v = 0°$, 20°, and 40°), as photographs show in the left panels of Figs. 6(c)–6(e). In the right panels, the corresponding ray-simulation results are presented, showing the visibility of the incident light (blue arrows), virtually divided into the seven regions (labeled as numbers 1–7). The mirror coating is indicated by thick black outlines. In the normal view of $\theta_v = 0°$ [Fig. 6(c)], the two center HR columns with the full mirror coating are invisible, which is confirmed by the ray-tracing simulation result (right) showing the representative light paths of *a-b-c-d-e* (red arrows) with the even number of reflections from the mirrors. The perspective view of the system is shown in Fig. 1(e). Note that the neck areas of the front resonators are visible (i.e., vertical thin black lines), but may be reduced by further optimizing the design of the resonators (e.g., moving the necks from the longitudinal vertices to the lateral vertices). As the view angle increases ($\theta_v = 20°$, and 40°), the rebuilt image is degraded due to a lack of information (1,3,5,7) and the wrong position of the projected information (2,4,6) [Figs. 6(d) and 6(e)]. Note that depending on application scenarios, reducing the visible-light blocking area would be beneficial when image information (such as sky and townscapes) is less important.

IV. CONCLUSIONS

We demonstrate an ultrasparse acoustic absorber that uses degenerate resonances with an asymmetric loss for perfect absorption. Such a systematic loss inclusion allows us to construct an absorber of a simple structure, which can be readily reconfigured for target applications. Ultrahigh sparsity enabled by increased absorption cross section is useful in many applications that require minimal flow resistance and good visibility. We present two additional capabilities: fluid flow and visible-light controls. Thus, our results open new directions of research by proposing the usefulness of multidisciplinary, multifunctional acoustic metamaterials.

APPENDIX A: DERIVATION OF EQ. (2)

By using the vibration amplitude ratio of $X_{ij} = x_i/x_j$, the damping matrix of Eq. (1) can be modified into a diagonal matrix as

$$\begin{bmatrix} \eta_l + \eta_r + \eta_c X_{21} & 0 \\ 0 & \eta_r + \eta_c X_{12} \end{bmatrix}, \tag{A1}$$

where the equality of $\eta_c(dx_2/dt) = \eta_c X_{21}(dx_1/dt)$ is used. We assume the $e^{-i\omega t}$ convention. In the frequency domain, Eq. (1) with the diagonal damping matrix ($S1$) gives $x_1(\omega)$:

$$\begin{aligned} x_1(\omega) &= \frac{F_1(\omega)}{m} \frac{1}{\left(\frac{k}{m} - \omega^2\right) - i\frac{1}{m}(\eta_l + \eta_r + \eta_c X_{21})\omega} \\ &= \frac{F_1(\omega)}{m} \frac{1}{\left[\omega_0^2 - \omega^2 + \mathrm{Im}\left(\frac{\eta_r + \eta_c X_{21}}{m}\right)\omega\right] - i\frac{1}{m}[\eta_l + \mathrm{Re}(\eta_r + \eta_c X_{21})]\omega}. \end{aligned} \tag{A2}$$

Similarly, $x_2(\omega)$ is given by

$$x_2(\omega) = \frac{F_2(\omega)}{m} \frac{1}{\left(\frac{k}{m} - \omega^2\right) - i\frac{1}{m}(\eta_r + \eta_c X_{12})\omega}. \tag{A3}$$

Using Eqs. (A2) and (A3), X_{21} is expressed by

$$X_{21} = \frac{x_2(\omega)}{x_1(\omega)} = F_{21} \frac{(\omega_0^2 - \omega^2) - i\frac{1}{m}(\eta_l + \eta_r + \eta_c X_{21})\omega}{(\omega_0^2 - \omega^2) - i\frac{1}{m}(\eta_r + \eta_c X_{12})\omega}. \tag{A4}$$

Rearranging Eq. (A4) leads to an explicit formula of X_{21} [Eq. (2b)], given by

$$\begin{aligned} X_{21} &= \frac{x_2(\omega)}{x_1(\omega)} \\ &= \left[\frac{(-\omega/\omega_0 + \omega_0/\omega)\eta_0 + 2i(\eta_l + \eta_r - F_{12}\eta_c)}{(-\omega/\omega_0 + \omega_0/\omega)\eta_0 + 2i(\eta_r - F_{21}\eta_c)}\right] F_{21}, \end{aligned} \tag{A5}$$

with $F_{ij} = F_i(\omega)/F_j(\omega)$.

From Eq. (A2), the dissipation power of the oscillator, averaged over a period, is given by

$$\begin{aligned} P_{\mathrm{diss}} &= \frac{1}{2}\frac{\eta_l}{\eta_l+\eta_r+\eta_c X_{21}}\mathrm{Re}\left[F_1^*(t)\frac{dx_1(t)}{dt}\right] \\ &= \frac{1}{2}\frac{\eta_l}{\eta_l+\eta_r+\eta_c X_{21}}\omega\,\mathrm{Im}[F_1^*(\omega)x_1(\omega)] \\ &= \frac{2\frac{\eta_l}{\eta_0}\frac{\alpha_1^2|p(\omega)|^2S_{\mathrm{osc}}^2}{\eta_0}\omega_0^2\omega^2}{\left[\omega_0^2-\omega^2+\mathrm{Im}\left(\frac{\eta_r+\eta_c X_{21}}{m}\right)\omega\right]^2+4\left[\frac{\eta_l}{\eta_0}+\mathrm{Re}\left(\frac{\eta_r+\eta_c X_{21}}{\eta_0}\right)\right]^2\omega_0^2\omega^2}, \end{aligned} \tag{A6}$$

where we have used $F(\omega) = \alpha_1 p(\omega)S_{\mathrm{osc}}$, $\eta_0 = 2\sqrt{km}$, and $\omega_0 = \sqrt{k/m}$. The incident acoustic power is written as

$$P_{\mathrm{inc}} = \frac{1}{2}\frac{|p(\omega)|^2S_{\mathrm{inc}}}{Z}. \tag{A7}$$

Using Eqs. (A6) and (A7) with the equality of $\eta_r^o = ZS_{\mathrm{osc}}^2/S_{\mathrm{inc}}$, the absorption (power) coefficient, defined as the ratio of the powers $P_{\mathrm{diss}}/P_{\mathrm{inc}}$, is determined as

$$\begin{aligned} A(\omega) &= \frac{4\alpha_1^2\left(\frac{\eta_r^o}{\eta_0}\frac{\eta_l}{\eta_0}\right)\omega^2\omega_0^2}{\left(\omega^2-\omega_0^2+2\mathrm{Im}\left(\frac{\eta_r+\eta_c X_{21}}{\eta_0}\right)\omega\omega_0\right)^2+4\left(\frac{\eta_l}{\eta_0}+\mathrm{Re}\left(\frac{\eta_r+\eta_c X_{21}}{\eta_0}\right)\right)^2\omega^2\omega_0^2} \\ &= \frac{4\alpha_1^2\left(\frac{\eta_r^o}{\eta_0}\frac{\eta_l}{\eta_0}\right)}{\left(\frac{\omega}{\omega_0}-\frac{\omega_0}{\omega}+2\,\mathrm{Im}\left(\frac{\eta_r+\eta_c X_{21}}{\eta_0}\right)\right)^2+4\left(\frac{\eta_l}{\eta_0}+\mathrm{Re}\left(\frac{\eta_r+\eta_c X_{21}}{\eta_0}\right)\right)^2}. \end{aligned} \tag{A8}$$

Eq. (2) is obtained from Eq. (A8) by assuming $\alpha_1 = 1$. This assumption is valid for subwavelength resonators.

APPENDIX B: NUMERICAL RETRIEVAL OF LEAKAGE LOSS (η_R) AND RADIATION COUPLING (η_C)

The leakage loss of resonators is equivalent to radiation damping η_r (or multiplication of radiation impedance, Z_r, with the surface area of resonators, S_{osc}, i.e., $\eta_r = Z_r S_{\mathrm{osc}}$). Physically, the leakage loss corresponds to the radiation impedance acting on the vibrating surface. For a resonator vibrating with $U_0e^{-i\omega t}$ in the absence of incident acoustic waves (Fig. 7), radiation damping η_r is calculated with radiation force on the resonator (its area of S_1) by

$$\eta_r = \frac{\int_{S_1} p_r dS}{U_0 e^{-i\omega t}}, \tag{B1}$$

where p_r is the pressure field induced by the vibrating resonator. For an isolated resonator, p_r is given by

$$p_r = \int_{S_1}\frac{iZk}{2\pi r}U_0 e^{-i(\omega t-\gamma r)}dS, \tag{B2}$$

where r is the distance from the surface of the resonator and γ is the wave number. In this case, an analytical form of η_r may be simply obtained. However, in the case of a periodic structure, the analytical form of radiation damping is complicated because p_r needs to be calculated by full modal expansion with the periodic boundary condition. Thus, the radiation damping η_r reflects the periodic nature of a resonator array (coupling between resonators). For convenience, we have numerically retrieved the radiation damping.

Similarly, radiation coupling η_c is determined by

$$\eta_c = \frac{\int_{S_2} p_r dS}{U_0 e^{-i\omega t}}. \tag{B3}$$

The difference from η_r is that the integration is conducted over the bottom surface area (S_2) where the back resonators are placed, since the radiation coupling relates to the coupling between the front and back resonators.

These two terms are easily calculated from numerical calculations (COMSOL), where we have used a lossless harmonic oscillator with the periodic boundary condition, as illustrated in Fig. 7. In the absence of incident acoustic waves, the oscillator is driven by an external body force (harmonic). The radiation pressure field is generated by the vibrating oscillator such that it is integrated over S_1 and S_2 for radiation damping and radiation coupling, respectively. Finally, the integrated pressure is divided by the velocity of the vibrating oscillator. Note that in the numerical calculation, the back resonator is not placed because the two terms are based on the radiation pressure field induced by either of the two resonators. By reciprocity, the two terms by the back resonator are the same as those by the front resonator.

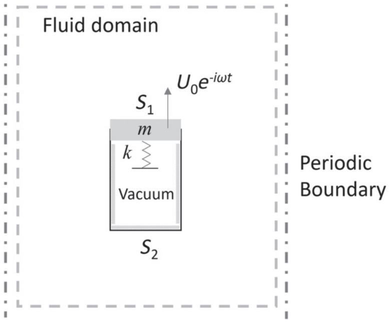

FIG. 7. Lossless harmonic oscillator model for numerical retrieval of η_r and η_c. Periodic boundary conditions are applied to the left and right boundaries, while radiation boundary conditions are applied to the top and bottom boundaries. The rigid mass (m) on top of the rectangular is harmonically excited, and its top surface interacts with the fluid domain. The spring attached to the rigid mass is modeled by using a spring boundary condition without using a physical structure.

[1] S. A. Cummer, J. Christensen, and A. Alù, Controlling sound with acoustic metamaterials, Nat. Rev. Mater. **1,** 16001 (2016).

[2] G. Ma and P. Sheng, Acoustic metamaterials: From local resonances to broad horizons, Sci. Adv. **2,** 1501595 (2016).

[3] L. Zigoneanu, B. I. Popa, and S. A. Cummer, Three-dimensional broadband omnidirectional acoustic ground cloak, Nat. Mater. **13,** 352 (2014).

[4] N. Fang, D. Xi, J. Xu, M. Ambati, W. Srituravanich, C. Sun, and X. Zhang, Ultrasonic metamaterials with negative modulus, Nat. Mater. **5,** 452 (2006).

[5] J. Li, L. Fok, X. Yin, G. Bartal, and X. Zhang, Experimental demonstration of an acoustic magnifying hyperlens, Nat. Mater. **8,** 931 (2009).

[6] R. Fleury, D. Sounas, and A. Alu, An invisible acoustic sensor based on Parity-Time symmetry, Nat. Commun. **6,** 5905 (2015).

[7] T. Liu, X. Zhu, F. Chen, S. Liang, and J. Zhu, Unidirectional Wave Vector Manipulation in Two-Dimensional Space with an all Passive Acoustic Parity-Time-Symmetric Metamaterials Crystal, Phys. Rev. Lett. **120,** 124502 (2018).

[8] P. Wei, C. Croënne, S. T. Chu, and J. Li, Symmetrical and anti-symmetrical coherent perfect absorption for acoustic waves, Appl. Phys. Lett. **104,** 121902 (2014).

[9] J. Z. Song, P. Bai, Z. H. Hang, and Y. Lai, Acoustic coherent perfect absorbers, New J. Phys. **16,** 033026 (2014).

[10] V. Romero-García, G. Theocharis, O. Richoux, A. Merkel, V. Tournat, and V. Pagneux, Perfect and broadband acoustic absorption by critically coupled sub-wavelength resonators, Sci. Rep. **6,** 19519 (2016).

[11] N. Jiménez, V. Romero-García, V. Pagneux, and J.-P. Groby, Rainbow-trapping absorbers: Broadband, perfect and asymmetric sound absorption by subwavelength panels for transmission problems, Sci. Rep. **7,** 13595 (2017).

[12] H. Long, Y. Cheng, J. Tao, and X. Liu, Perfect absorption of low-frequency sound waves by critically coupled subwavelength resonant system, Appl. Phys. Lett. **110,** 023502 (2017).

[13] J. Mei, G. Ma, M. Yang, Z. Yang, W. Wen, and P. Sheng, Dark acoustic metamaterials as super absorbers for low-frequency sound, Nat. Commun. **3,** 756 (2012).

[14] M. Yang, C. Meng, C. Fu, Y. Li, Z. Yang, and P. Sheng, Subwavelength total acoustic absorption with degenerate resonators, Appl. Phys. Lett. **107,** 104104 (2015).

[15] A. Merkel, G. Theocharis, O. Richoux, V. Romero-Garcia, and V. Pagneux, Control of acoustic absorption in one-dimensional scattering by resonant scatterers, Appl. Phys. Lett. **107,** 244102 (2015).

[16] Y. Li and B. M. Assouar, Acoustic metasurface-based perfect absorber with deep subwavelength thickness, Appl. Phys. Lett. **108,** 063502 (2016).

[17] J. Li, W. Wang, Y. Xie, B.-I. Popa, and S. A. Cummer, A sound absorbing metasurface with coupled resonators, Appl. Phys. Lett. **109,** 091908 (2016).

[18] N. Jiménez, V. Romero-García, V. Pagneux, and J.-P. Groby, Ultra-thin metamaterial for perfect and quasi-omnidirectional sound absorption, Appl. Phys. Lett. **109,** 121902 (2016).

[19] Y. Tang, S. Ren, H. Meng, F. Xin, L. Huang, T. Chen, C. Zhang, and T. J. Lu, Hybrid acoustic metamaterial as super absorber for broadband low-frequency sound, Sci. Rep. **7,** 43340 (2017).

[20] M. Yang, S. Chen, C. Fu, and P. Sheng, Optimal sound-absorbing structures, Mater. Horiz. **4,** 673 (2017).

[21] T. Lee and H. Iizuka, Heavily overdamped resonance structurally engineered in a grating metasurface for ultra-broadband acoustic absorption, Appl. Phys. Lett. **113,** 101903 (2018).

[22] J. Kang and M. W. Brocklesby, Feasibility of applying micro-perforated absorbers in acoustic window systems, Appl. Acoust. **66,** 669 (2005).

[23] Y. Cheng, C. Zhou, B. G. Yuan, D. J. Wu, Q. Wei, and X. J. Liu, Ultra-sparse metasurface for high reflection of low-frequency sound based on artificial Mie resonances, Nat. Mater. **14,** 1013 (2015).

[24] X. Wu, K. Y. Au-Yeung, X. Li, R. C. Roberts, J. Tian, C. Hu, Y. Huang, S. Wang, Z. Yang, and W. Wen, High-efficiency ventilated metamaterial absorber at low frequency, Appl. Phys. Lett. **112,** 103505 (2018).

[25] C. Shen, Y. Xie, S. A. Cummer, and Y. Jing, Omnidirectional sound shielding with acoustic metacages, J. Acoust. Soc. Am. **141,** 3574 (2017).

[26] J. R. Piper, V. Liu, and S. Fan, Total absorption by degenerate critical coupling, Appl. Phys. Lett. **104,** 251110 (2014).

[27] L. C. Botten, R. C. McPhedran, N. A. Nicorovici, and G. H. Derrick, Periodic models for thin optimal absorbers of electromagnetic radiation, Phys. Rev. B **55,** R16072 (1997).

[28] H. Long, S. Gao, Y. Cheng, and X. Liu, Multiband quasi-perfect low-frequency sound absorber based on double-channel Mie resonator, Appl. Phys. Lett. **112,** 033507 (2018).

[29] Z. Ruan and S. Fan, Superscattering of Light from Subwavelength Nanostructures, Phys. Rev. Lett. **105,** 013901 (2010).

[30] See Supplemental Material at http://link.aps.org/supplemental/10.1103/PhysRevApplied.11.024022 for videos of fluid flow control, schematics of experimental setups, and additional figures and notes.

[31] S. S. Rao, *Mechanical Vibrations* (Prentice Hall, Upper Saddle River, 2011), 5th ed.

[32] V. Achilleos, G. Theocharis, O. Richoux, and V. Pagneux, Non-Hermitian acoustic metamaterials: Role of exceptional points in sound absorption, Phys. Rev. B **95,** 144303 (2017).

[33] T. Mellow and L. Karkkainen, On the sound fields of infinitely long strips, J. Acoust. Soc. Am. **130,** 153 (2011).

[34] V. Leroy, A. Strybulevych, M. Lanoy, F. Lemoult, A. Tourin, and J. H. Page, Superabsorption of acoustic waves with bubble metascreens, Phys. Rev. B **91,** 020301(R) (2015).

[35] H. J. Lezec, A. Degiron, E. Devaux, R. A. Linke, L. Martin-Moreno, F. J. Garcia-Vidal, and T. W. Ebbesen, Beaming light from a subwavelength aperture, Science **297,** 820 (2002).

[36] S. Carretero-Palacios, O. Mahboub, F. J. Garcia-Vidal, L. Martin-Moreno, S. G. Rodrigo, C. Genet, and T. W. Ebbesen, Mechanisms for extraordinary optical transmission through bull's eye structure, Opt. Express **19,** 10429 (2011).

[37] D. A. Russell, J. P. Titlow, and Y.-J. Bemmen, Acoustic monopoles, dipoles, and quadrupoles: An experiment revisited, Am. J. Phys. **67**, 660 (1999).

[38] L. Verslegers, Z. Yu, Z. Ruan, P. B. Catrysse, and S. Fan, From Electromagnetically Induced Transparency to Superscattering with a Single Structure: A Coupled-Mode Theory for Doubly Resonant Structures, Phys. Rev. Lett. **108**, 083902 (2012).

[39] Y. Duan, J. Luo, G. Wang, Z. H. Hang, B. Hou, J. Li, P. Sheng, and Y. Lai, Theoretical requirements for broadband perfect absorption of acoustic waves by ultra-thin elastic meta-films, Sci. Rep. **5**, 12139 (2015).

[40] A. Vora, J. Gwamuri, N. Pala, A. Kulkarni, J. M. Pearce, and DÖ Güney, Exchanging ohmic losses in metamaterial absorbers with useful optical absorption for photovoltaics, Sci. Rep. **4**, 4901 (2014).

[41] J. Hao, J. Wang, X. Liu, W. J. Padilla, L. Zhou, and M. Qiu, High performance optical absorber based on a plasmonic metamaterial, Appl. Phys. Lett. **96**, 251104 (2010).

[42] P. B. S. Lissaman, Low-Reynolds-number airfoils, Annu. Rev. Fluid Mech. **15**, 223 (1983).

[43] N. C. DeJong and A. M. Jacobi, Flow, heat transfer, and pressure drop in the near-wall region of louvered-fin arrays, Exp. Therm. Fluid Sci. **27**, 237 (2003).

[44] J. B. Pendry, D. Schurig, and D. R. Smith, Controlling electromagnetic fields, Science **312**, 1780 (2006).

[45] U. Leonhardt, Optical conformal mapping, Science **312**, 1777 (2006).

[46] L. Xu and H. Chen, Conformal transformation optics, Nat. Photonics **9**, 15 (2015).

[47] X. Chen, Y. Luo, J. Zhang, K. Jiang, J. B. Pendry, and S. Zhang, Macroscopic invisibility cloaking of visible light, Nat. Commun. **2**, 176 (2011).

[48] D. Banerjee, C. Ji, and H. Iizuka, Invisibility cloak with image projection capability, Sci. Rep. **6**, 38965 (2016).